dynamics

Article

Dynamic Plasticity and Fracture of Al 7075 and V95T1 Alloys: High-Velocity Impact Experiments

Egor S. Rodionov, Andrey Ya. Cherepanov, Alfiya G. Fazlitdinova, Timur T. Sultanov, Victor G. Lupanov, Polina N. Mayer and Alexander E. Mayer *

Department of General and Theoretical Physics, Chelyabinsk State University, 454001 Chelyabinsk, Russia; rodionoves.pgd@gmail.com (E.S.R.); cherepanov.andrej174@gmail.com (A.Y.C.); fazlitdinovaag@mail.ru (A.G.F.); tima242003@mail.ru (T.T.S.); victr@csu.ru (V.G.L.); polina.nik@mail.ru (P.N.M.)

* Correspondence: mayer@csu.ru

Abstract: A novel method to measure dynamic flow stress and corresponding strain rates obtained from Taylor tests using profiled samples with a reduced cylindrical head part was applied to study the dynamic characteristics of similar commercial 7075 and V95T1 aluminum alloys. The measured dynamic flow stress is verified using a classical Taylor's approach with uniform cylinders and compared with the literature data. Our study shows that the dynamic flow stress of 7075 alloy, which is 786 MPa at strain rates of (4–8) $\times$ 10^3 s^{-1}, exceeds the value of 624 MPa for V95T1 alloy at strain rates of (2–6) $\times$ 10^3 s^{-1} by 25%. The threshold impact velocity resulting in fracture of the 4 mm head part of the profiled samples is 116–130 m/s for 7075 alloy and only 108 m/s for V95T1 alloy. The fracture pattern is also different between the alloys with characteristic shear-induced cracks oriented at 45° to the impact direction in the case of V95T1 alloy and perpendicular to the breaking off head part in the case of 7075 alloy. On the other hand, the compressive fracture strain of V95T1 alloy, which is 0.29–0.36, exceeds that of 7075 alloy, which is 0.27–0.33, by approximately 8%. Thus, V95T1 aluminum alloy exhibits less strength but is more ductile, while 7075 aluminum alloy exhibits more strength but is simultaneously more brittle.

Keywords: dynamic deformation; dynamic fracture; dynamic flow stress; Taylor impact test; 7075 and V95T1 alloys; analytical estimate

check for updates

Academic Editor: Christos Volos

Received: 2 January 2025
Revised: 7 February 2025
Accepted: 11 February 2025
Published: 15 February 2025

Citation: Rodionov, E.S.; Cherepanov, A.Y.; Fazlitdinova, A.G.; Sultanov, T.T.; Lupanov, V.G.; Mayer, P.N.; Mayer, A.E. Dynamic Plasticity and Fracture of Al 7075 and V95T1 Alloys: High-Velocity Impact Experiments. *Dynamics* **2025**, *5*, 6. https://doi.org/10.3390/dynamics5010006

1. Introduction

Despite the significant development of theoretical models and numerical simulations in the field of solid mechanics, conducting full-scale experiments on material deformation will remain a relevant task for a long time. A full-scale experiment allows one to study the mechanical response of a material under quasi-static or dynamic loading, which is essential for industrial applications. Dynamic loading is widespread in industrial manufacturing processes, such as high-speed machining and thermo-mechanical treatment, as well as in operation conditions, especially in aerospace, transportation, and defense areas. The existence of a large number of metallic materials in various structural states and the continuous development of new materials makes relevant the development of robust, but simple and cheap methods for experimental dynamic testing.

There are a lot of experimental techniques that can be used in combination to allow one to study the properties of a material in a wide range of strain rates. Split Hopkinson–Kolsky bars provide material strain rates up to 10^4 s^{-1} [1–3] and allow obtaining stress–strain curves up to the fracture strain. Experiments with the generation of plane shock waves obtained with high-velocity plate impacts [4–7] allow interpreting measurements of the dynamic plasticity and spall strength of materials by recording the velocity of the back surface of the plate using laser interferometry [8]. Such experiments make it possible to cover strain rates from 10^4 to 10^7 s^{-1} depending on the thicknesses of the sample and impactor. Covering this wide range of strain rates, this method is restricted based on imposed total deformation. One of the simplest and most accessible methods to study the dynamic deformation of materials in the range of strain rates of 10^3–10^5 s^{-1} and with strain values of approximately or exceeding one is the Taylor anvil-on-rod test [9–13]. This technique classically involves the impact of a uniform cylindrical sample with a rigid barrier and subsequent analysis of the modified geometry of the impactor in order to study the dynamic properties of the material, namely, the dynamic yield strength.

Although the Taylor test was first proposed in 1948 [14], it is still widely used for the assessment of dynamic properties of traditional and novel materials, as well as for material model verification and parameterization [15–18]. Further simplification of the experimental procedure and data processing with extension of the strain rate range makes sense. For instance, modification of the sample shape with profiling of the head part allowed us to concentrate the impact energy and material deformation in the head part and to reach strain rates of up to 10^5 s^{-1} at restricted impact velocities of 100–150 m/s [16], making the dynamic testing even more simple and accessible. Such experiments provide additional data for parameterization of the dynamic plasticity and fracture models using the machine-learning approach [16,18]. In addition, a method for direct measurement of average values of the dynamic flow stress and strain rate using only the change in length of the impacted sample was proposed and verified in [19] for the case of profiled samples with a reduced cylindrical head part. Here, we apply this novel method together with the classical one proposed in [14] to study the dynamic flow stress and fracture characteristics of two similar high-strength aluminum alloys: (i) 7075 alloy according to the US and EU classification that is produced in China and (ii) V95T1 alloy produced in Russia that is a domestic analogue of the first one.

Parts made from the high-strength aluminum alloys (7075 and V95T1) are known to be comparable in strength to some types of steel, while being resistant to corrosion. The combination of mechanical and chemical properties of the material allows it to be used in various civilian and military areas, such as mechanical engineering, aircraft construction [20], rocket science, etc. In addition to aircraft and rocketry, these alloys are used to make bushings, frames and hubs for bicycles, car suspension arms, and chain rings, and, recently, there is a tendency to manufacture connecting rod mechanisms for car engines. In spite of the long history of the alloys, such diverse applications make relevant the study of mechanical properties under various conditions and for various initial microstructural states, which is supported by a large number of recent papers. Specifically, the plasticity at increased temperatures [21–23] and various previous heat treatments [24], the properties of additively manufactured samples [25], and the ballistic performance of 7075 aluminum alloy [26,27] are being actively studied. The study of plastic deformation and fracture under dynamic loading is of particular interest. One of the significant drawbacks of the alloys is the tendency for microsegregation [28] (uneven distribution of alloying and impurity elements in the alloy after its solidification), which can lead to its embrittlement in a local area of the sample, affecting its dynamic properties and limiting plastic deformation.

This work has three objectives: (i) to collect experimental data for further parameterization of the dynamic plasticity and fracture models using a machine-learning approach similar to that described in [16,18]; (ii) to apply the novel method of direct processing of the experimental data [19] and compare the obtained dynamic flow stress with the literature data; and (iii) to compare dynamic properties of two similar high-strength aluminum alloys (7075 and V95T1). These three points explain the novelty of the present study. The structure of paper is as follows. Section 2 describes the experimental methods and the processing of experimental results to calculate the dynamic flow stress. Section 3 presents the experimental results, including the shapes and lengths of deformed samples, as well as fractography of fracture surfaces. Section 4 discusses the obtained values of dynamic flow stress, strain rate, and fracture strain values in comparison with the literature data, while Section 5 concludes our study.

2. Materials and Methods

2.1. Materials, Samples, and High-Pressure Gas Gun

In the present paper, we compare dynamic response of a commercial aluminum alloy of grade 7075 produced in China and its Russian analog of grade V95T1. The chemical compositions of both alloys with zinc, magnesium, and copper as the main alloying elements are close as shown in Table 1. This table shows elemental composition according to both specification data and measurements for particular tested samples. The measurements are performed at five local points using a Jeol 6590LA scanning electron microscope (JEOL Ltd., Tokyo and Akishima, Japan) equipped with an energy dispersive spectrometer. Large scatter of the measured element concentrations correlate with the known issue of microsegregation for this type of aluminum alloy [28]. All measured average values of concentrations are within the ranges defined by the specifications except that for Si, which reveals an exceptionally non-uniform distribution. Non-uniform distribution of Si in aluminum alloys leads to their embrittlement.

Table 1. Chemical composition of 7075 and V95T1 alloys.

Element	Al 7075		V95T1	
	Specification	Measured	Specification	Measured
Al, %	87.1–91.4	89.4 $\pm$ 2	86.3–91	91.0 $\pm$ 2.5
Zn, %	5.1–6.1	5.5 $\pm$ 2.5	5–7	4.9 $\pm$ 2
Mg, %	2.1–2.9	2.3 $\pm$ 0.5	1.8–2.8	1.8 $\pm$ 0.4
Cu, %	1.2–2.0	1.7 $\pm$ 1.2	1.4–2	1.5 $\pm$ 1.2
Si, %	0.4	1.1 $\pm$ 1.6	0.5	0.9 $\pm$ 1.0

In both cases, the as-received material was supplied in the form of rods that were 8 mm in diameter. We conducted experimental studies on the dynamic impact of aluminum alloy samples with a rigid anvil made of stainless steel. Samples with the following shapes were cut from the 8 mm diameter as-received rods: (i) a classical uniform 8 mm cylinder, 40 mm in length, and (ii) a profiled cylinder with the same total length, but with a reduced (machined) head part with a diameter of 4 mm and a length of 10 mm as shown in Figure 1. A total of 12 samples of each type were prepared using a manual feed lathe; most of the samples were subjected to dynamic tests at different impact velocities, while some were used for preliminary tests and control purposes. Profiling the head of the cylinder was proposed in [16,18] and allowed increasing the strain and strain rate in the head part due to the impact energy concentration here [16] and reaching the fracture threshold [18]. In addition, an analytical estimation of the dynamic flow stress was proposed in [19] for the samples with the reduced cylindrical head part.

The samples were launched using an air gas gun with a maximum pressure excess of 10 bar above atmospheric in a high-pressure chamber. Impact velocities were up to 175 m/s. The installation for dynamic testing consists of a shock tube and a high-pressure chamber, see Figure 2a. A polypropylene tube with an internal diameter of 12 mm, in which the projectile was accelerated, was placed inside the shock tube. The metal case of the shock tube was used as a protection shield, as well as for reducing the pressure ahead of the accelerated sample. For this purpose, air was evacuated from the working section of the shock tube to a pressure of 0.01 bar using a vacuum pump, which reduced the frontal air resistance of the projectile and increased the impact velocity. The velocity was measured using the time-of-flight method. The transition cuff, Figure 2c, connected the pumping chamber and the polypropylene tube, which had different diameters, directing compressed air into the polypropylene tube and preventing leakage into the working section of the shock tube. The plastic transition cuff was manufactured using a 3D printer, and the printing technology is FDM (Fused Deposition Modeling). To prevent bending of the polypropylene tube and to ensure normal impact of the samples with the anvil, a centering system is placed inside the shock tube consisting of steel rods interconnected by plastic rings manufactured using a 3D printer, see Figure 2b,d.

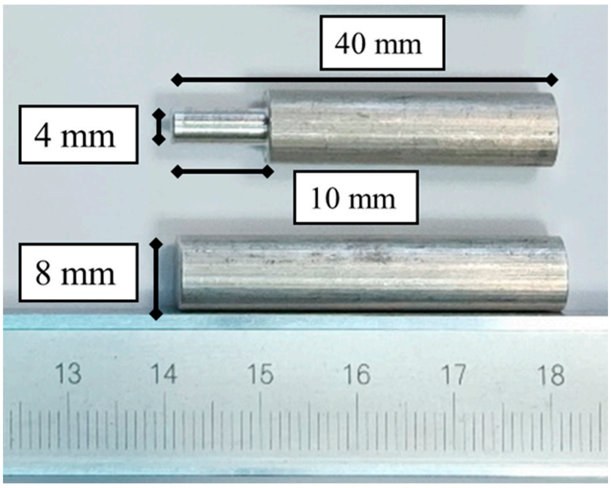

Figure 1. Initial shapes of the aluminum impactors used in the Taylor tests.

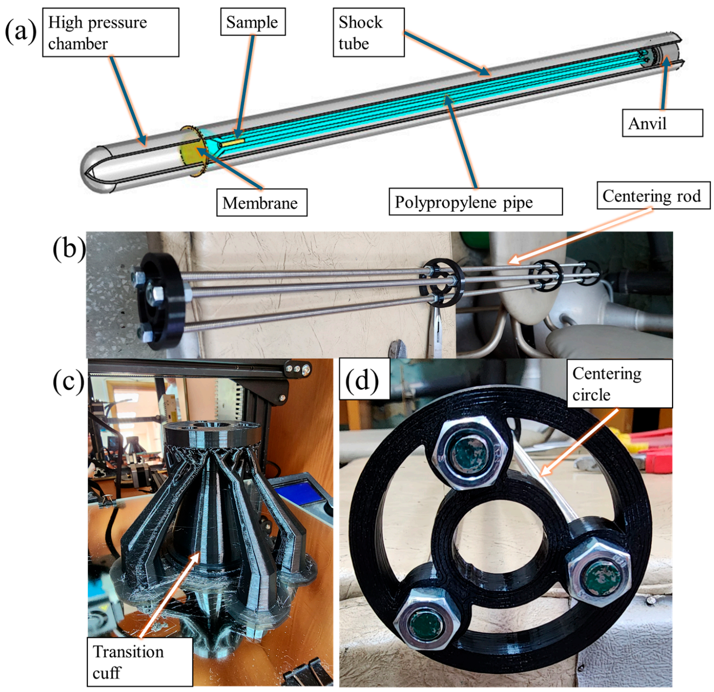

Figure 2. Experimental setup: (**a**) Schematic representation of the shock tube design; (**b**) Centering system, which serves to ensure normal impact; (**c**) Transition cuff, directing the pressure from the pumping chamber into the polypropylene tube; (**d**) Centering ring, which is the main element of the centering system.

2.2. Estimation of Dynamic Flow Stress with Profiled Impactors

Here, we consider a simple method previously proposed in [19] for estimating the dynamic flow stress, the stopping time, and the average strain rate in the case of profiled impactors with a reduced cylindrical head part. This method was verified in [19] against 3D numerical simulations using an example of cold rolled copper. It was shown that the estimates are valid under conditions of deformation of only the profiled part of the cylinder, while the non-profile part should not experience deformation. This requirement is well fulfilled in the present experiments with high strength aluminum alloys. Specifically, the main part of the profiled cylinders is not deformed, but the profiled part is destroyed at high impact velocities. The method is explained here for the sake of completeness of the presentation.

The estimated characteristics are easy to obtain, as the initial L_{h0} and final L_{hf} lengths of the reduced head part as well as the total mass m of the sample and the impact velocity v_0 are known. An approximation of uniform deformation and uniform stresses in the reduced head part is introduced in [19] to get analytical expressions. If there is no deformation of the main part, then the kinetic energy of the impactor is completely spent on the plastic deformation of the head part or on the processes of crack formation and subsequent fracture. Here, we consider collision modes without fracture.

We assume that the constant axial stress equal to the dynamic flow stress Y acts in the head part during the impactor deceleration and that the radial stress is zero due to the lateral unloading. An incremental shortening dL_{h} of the head part with the current length L_{h} leads to an increase in axial deformation by $dL_{\mathrm{h}}/L_{\mathrm{h}}$. The work of axial stress on this deformation is equal to $Y(dL_{\mathrm{h}}/L_{\mathrm{h}})V_{\mathrm{h}}$, where V_{h} is the volume of the head part, which remains constant during the plastic deformation. The total work during the impactor stopping should be equal to the initial kinetic energy, which leads to the following expression for the dynamic yield stress [19]:

$$Y = mv_0^2\left[2V_{\mathrm{h}}\ln\left(\frac{L_{\mathrm{h0}}}{L_{\mathrm{hf}}}\right)\right]^{-1} \tag{1}$$

Using similar considerations, the following expression can be obtained for intermediate velocities v:

$$L_{\mathrm{h}} = L_{\mathrm{h0}}\exp\left[-\frac{m(v_0^2 - v^2)}{2YV_{\mathrm{h}}}\right] \tag{2}$$

Combining Equation (2) with the momentum conservation in the incremental form, the following is obtained:

$$mdv = -Y(V_{\mathrm{h}}/L_{\mathrm{h}})dt \tag{3}$$

where $V_{\mathrm{h}}/L_{\mathrm{h}}$ is an estimate for the current cross-sectional area of the head part valid for incompressible plastic flow. Making the corresponding integration, the following estimate for the stopping time was derived in [19]:

$$t_{\mathrm{f}} = \sqrt{\frac{\pi}{2}}L_{\mathrm{h0}}\sqrt{\frac{m}{YV_{\mathrm{h}}}}\exp\left(-\frac{mv_0^2}{2YV_{\mathrm{h}}}\right)\mathrm{erfi}\left(\sqrt{\frac{mv_0^2}{2YV_{\mathrm{h}}}}\right), \tag{4}$$

where $\mathrm{erfi}(\cdot)$ denotes the imaginary error function. If the total engineering strain of the sample head par is equal to $\varepsilon_{\mathrm{f}} = 1 - L_{\mathrm{hf}}/L_{\mathrm{h0}}$, the average strain rate can be calculated as follows:

$$\dot{\varepsilon} = \varepsilon_{\mathrm{f}}/t_{\mathrm{f}} = (1 - L_{\mathrm{hf}}/L_{\mathrm{h0}})/t_{\mathrm{f}} \tag{5}$$

Thus, Equation (1) estimates the dynamic flow stress, while Equations (4) and (5) estimate the corresponding strain rate. The simultaneous analytical estimation of the flow stress and strain rate using only the length of deformed sample is a unique feature of the profiled samples with the cylindrical reduced head part.

2.3. Estimation of Dynamic Flow Stress with Classical Uniform Cylinders

To estimate the dynamic tensile strength of classical uniform cylindrical impactors, we use the equation proposed by Taylor [14].

$$Y = \frac{\rho {v_0}^2}{2 \cdot \ln(L_0/X)} \frac{(L_0 - X)}{(L_0 - L_\mathrm{f})}, \quad (6)$$

where ρ is the density of examined material, L_0 is the initial total length of impactor, L_f is the final length after dynamic deformation, and X is length of the undeformed part of the sample after impact. For metals, two approaches can be used to determine the undeformed length X. The first one is to grind and polish each sample perpendicular to the plane of impact, etch it, and determine the boundary of the deformed region by the change in material microstructure. The second one is to apply micrometric measurements of diameter in a number of points along the impact direction to detect the change in the profile of the deformed sample. The second method is less accurate. However, due to its simplicity and the speed of calculating geometric parameters, it was used by us to calculate the undeformed length X.

3. Experimental Results

This section presents the experimental results on the dynamic deformation of samples made of aluminum alloys of Al 7075 and V95T1 grades. A comparison of deformation and fracture characteristics of these two similar alloys is performed. The results of scanning electron microscopy (SEM) of fracture surfaces are presented.

3.1. Deformation and Fracture Characteristics

Figures 3 and 4 show photographs of all dynamically tested classical cylindrical impactors that were 8 mm in diameter and 40 mm in length and profiled ones with a 4 mm in diameter head part, respectively. Both figures compare the cases of Al 7075 and V95T1 aluminum alloys in panels (a) and (b), respectively. Table A1 in Appendix A collects the measured geometric parameters of all deformed samples impacted without fracture, including the final lengths and diameters of impact edge.

Let us consider the classical cylinders in Figure 3 at first. For both alloys, as the impact velocity increases, the impact edge diameter monotonically increases, and the sample length decreases. At the same time, before reaching an impact velocity of approximately 120 m/s, the change in the sample diameter visually seems small. The key differences between the alloys are observed at high impact velocities of about 175 m/s. In the case of 7075 alloy, the process of nucleation of shear cracks up to 1 mm long is observed on the impact surface of the sample, but their number is small. When examining the V95T1 alloy, the formation of a large number of shear cracks up to several millimeters long is observed along the impact surface of the metal, and the onset of the process of material deformation was noted along the cavities that appeared. The formed cracks near the impact surface in V95T1 alloy are shown in Figure 5a. It can be concluded that the V95T1 alloy, at comparable impact velocities, is prone to a greater growth and number of defects leading to material failure than in the case of the 7075 alloy.

In the case of the profiled cylinders shown in Figure 4, the examined impact velocities are lower than in the case of 8 mm impactors since the head part of the sample is prone to fracture already at an impact velocity of about 110–120 m/s. It can be noted that, in the case of V95T1 alloy, the failure of the impactor head part is registered already at an impact velocity of 108 m/s. However, in the case of the 7075 alloy, the failure is observed at velocities of about 116 m/s. This observation correlates with the analysis of 8 mm cylinders, indicating a lower fracture threshold of V95T1 alloy. It should be mentioned that, similar to the case of brass [18], the fracture of the considered aluminum alloys is random in nature. Figure 4a shows two samples impacted at 116.3 m/s. One is fractured, while another one remains unbroken. However, a large crack is noted along the entire diameter of the profiled part at the transition point into the main cylinder. Besides, the sample impacted at 123.5 m/s was not fractured. At impact velocities above 140 m/s, significant fragmentation of the head part of the impactors is observed in the case of both alloys.

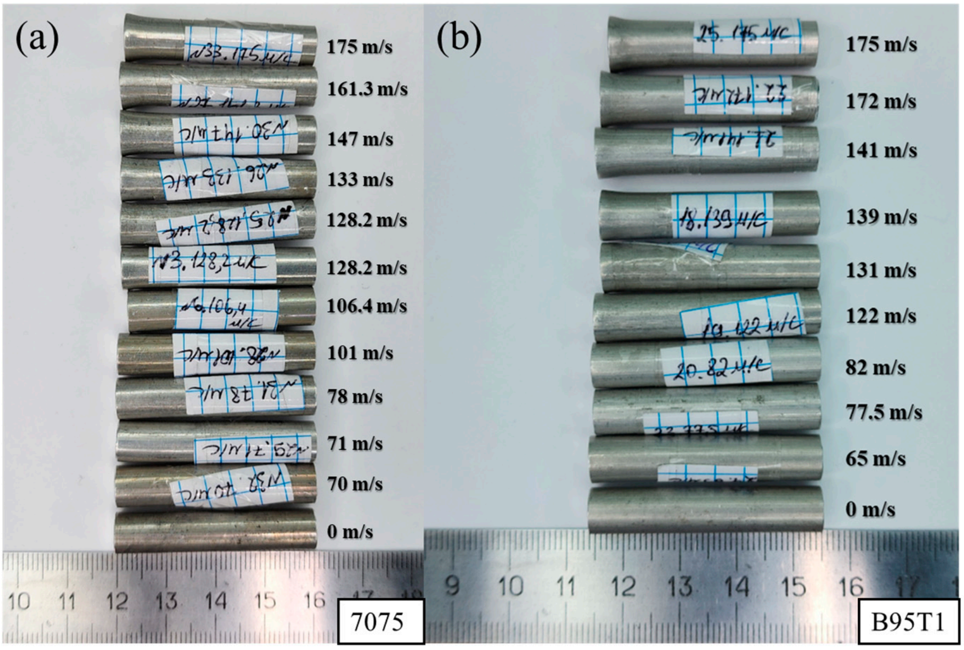

Figure 3. Photographs of classic cylindrical samples after dynamic testing: (**a**) Al7075 alloy; (**b**) V95T1 alloy.

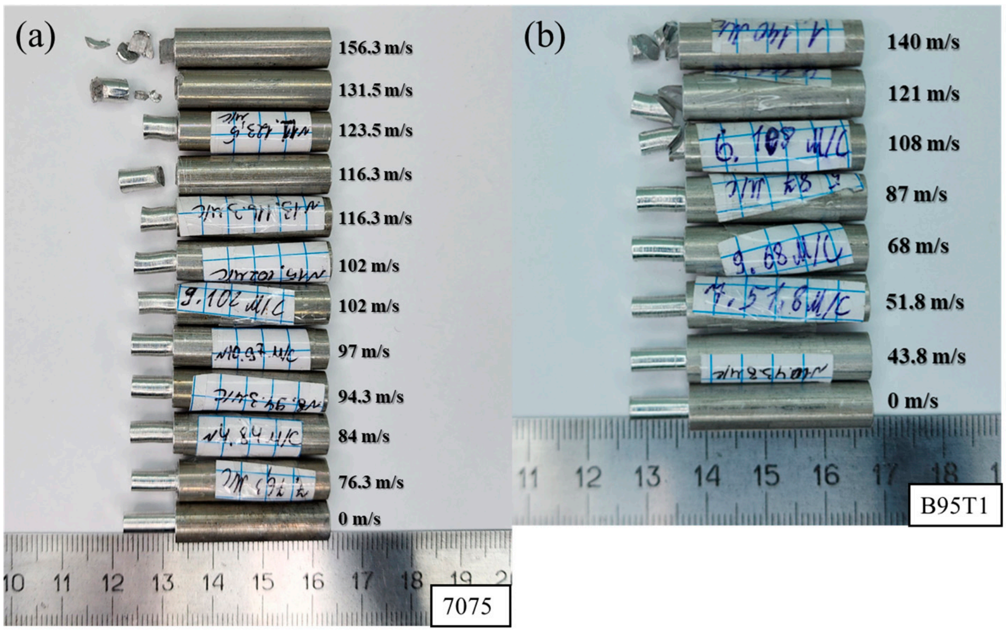

Figure 4. Photographs of profiled samples with a reduced head part after dynamic testing: (**a**) Al7075 alloy; (**b**) V95T1 alloy.

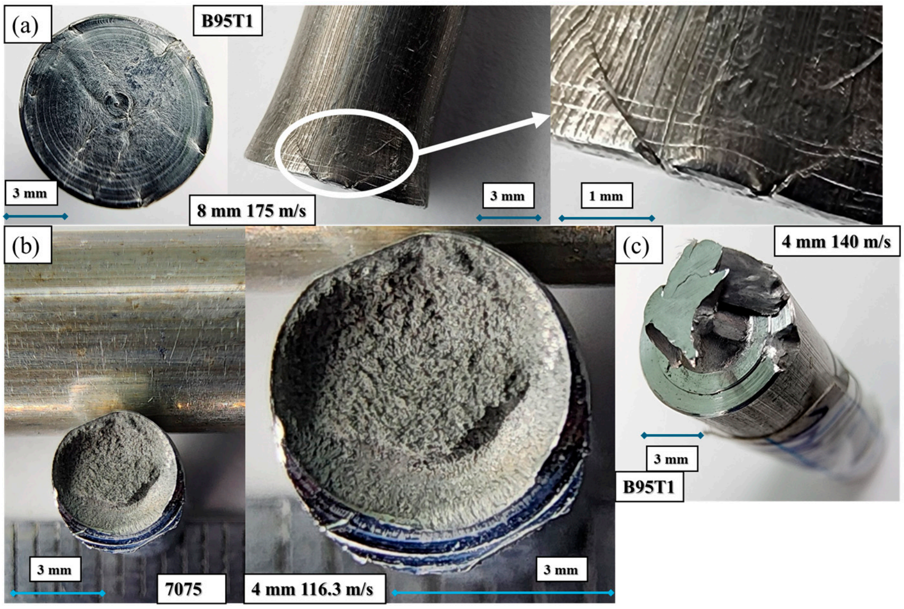

Figure 5. Photographs of the deformed impactors and their fractured parts: (**a**) Impact surface of classic 8 mm cylinder of V95T1 alloy, and the impact velocity is 175 m/s; (**b**) Broken-off head part of profiled 4 mm cylinder of 7075 alloy, and the impact velocity is 116.3 m/s; (**c**) Fracture surface of the profiled 4 mm impactor made of V95T1 alloy, and the impact velocity is 140 m/s.

The key difference between the alloys is the mode of fracture. In the case of V95T1 alloy, a classic phenomenon of brittle fracture of the material is observed along the direction of maximum shear stress. Similar cracks are also formed in the case of the 8 mm impactor of the same grade as discussed above. A characteristic feature is that the angle of propagation of the shear crack is approximately 45° relative to the impact direction; thus, the crack path coincides with the maximum shear stress direction. Even with an increase in the impact velocity and the formation of a large number of fragments, the base of the profiled part does not fracture, see Figure 5c. We encountered a similar type of fracture in the case of brass samples [18]. The fracture of profiled samples of 7075 alloy is significantly different. As can be seen from the photographs, there is a tendency for the profiled part to completely break away from the main cylinder, while the destroyed surface, see Figure 5b, externally resembles the appearance of rods that were destroyed by stretching them on a tensile testing machine. The fracture surface is completely covered with small pores, while there is no evidence of sliding of the broken head part on the sample surface, in contrast to the case of the V95T1 alloy. We have previously observed the initiation of this type of fracture in microstructural studies of profiled impactors made of hard cold rolled copper, in which the formation of a massive crack was observed at the transition point of the profiled part of the cylinder to the main part [16]. Such significant differences in the fracture processes prompted us to conduct a study of the fracture surfaces using SEM in Section 3.2.

Figure 6 shows the comparison of the geometric parameters of the dynamically deformed samples made of the studied alloys. The graphs show only the plastically deformed samples, including those with the small cracks; the fragmented samples are not shown. We present the geometric parameters in the normalized form, such as the ratio of the final length to the initial one and, similarly, the ratio of the final diameter of the impact edge to the initial one. This representation is meaningful because our previous molecular dynamics (MD) simulations [29] showed that these normalized parameters are substantially insensitive to size, which allows us to mitigate small fluctuations in the shape of the initial samples. Regarding high impact velocities of 8 mm classical cylinders as shown in Figure 6a,b, V95T1 alloy shows larger plastic deformation compared with 7075 alloy. This tendency is not so obvious for the profiled 4 mm samples in Figure 6c,d because the fracture of V95T1 samples occurs earlier than that for 7075 samples as discussed above. Remarkably, similar trends of the final length depending on the impact velocity described by second-order polynomials for classical cylinders and third-order polynomials for profiled cylinders are reported in [29] for both MD data for nano-sized samples and experimental data for millimeter-sized samples in the case of copper.

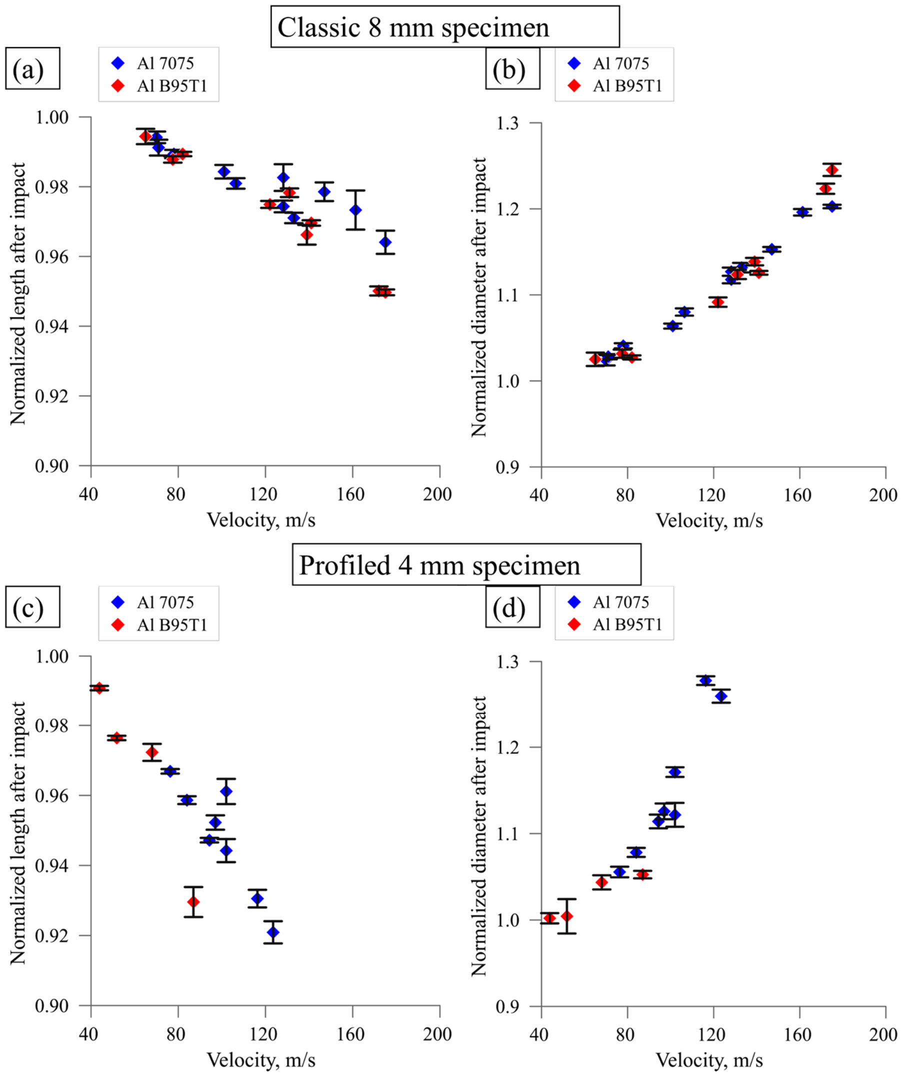

Figure 6. Experimental results: (**a**) Normalized length for classical 8 mm cylinders; (**b**) Normalized diameter for classical 8 mm cylinders; (**c**) Normalized length for profiled 4 mm cylinders; (**d**) Normalized diameter for profiled 4 mm cylinders. Normalization is performed with respect to the initial values before dynamic deformation. A comparison of data for 7075 alloy and V95T1 alloy is presented.

3.2. SEM Microscopy of Fracture Surfaces

The fracture surfaces of 4 mm profiled impactors were selected for SEM. The images are obtained using a Jeol 6590LA scanning electron microscope (JEOL Ltd., Tokyo and Akishima, Japan) at the accelerating voltage of 20 kV. SEM images of the fractured surfaces of samples made of V95T1 and 7075 alloys are shown in Figure 7 and Figure 8, respectively. In the case of the V95T1 alloy, a sliding surface of the specimen is observed, occupying about one-third of the fracture surface area, see Figure 7a. The remaining surface of the specimen apparently did not experience significant sliding during the fracture process. Small pores and material build-ups that form during the separation of the cylinder head part in the fracture process are visible; their microstructures are more similar to a wear surface [30]. In the case of the 7075 alloy specimen, the characteristic surface of a material that has experienced tensile loads is observed [30–33]. Characteristic stretched areas of the material with sharp boundaries containing a large number of micrometer-sized pores are observed. Figure 8d shows the fracture surface at low magnification of the scanning electron microscope. One can observe that the material rupture was uneven, as evidenced by multiple "steps" dividing the fracture surface of the material along the height. In addition, a large number of surface cracks are also observed on the fracture surface.

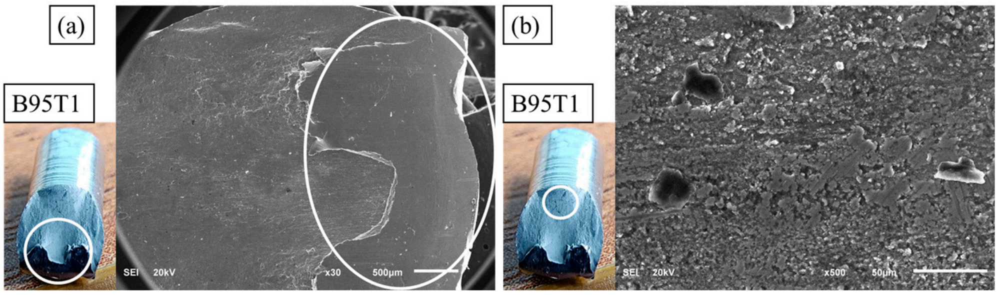

Figure 7. SEM fractograms of the fracture surface on the head part of V95T1 alloy with an impact velocity of 108 m/s: (**a**) Fracture surface with the white ellipse highlighting the fragment of material on which sliding occurred during fracture; (**b**) Enlarged photograph of the surface of the material that did not experience sliding during fracture. The studied areas are shown by the white circles in the photographs of the fractured head part of the impactor.

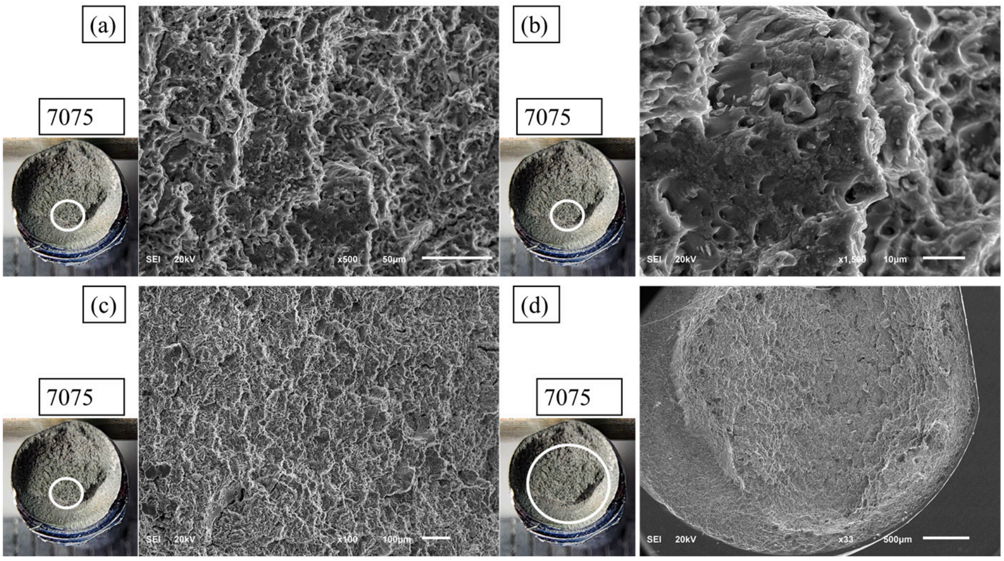

Figure 8. SEM fractograms of the fractured head part of 7075 alloy with an impact velocity of 116.3 m/s: (**a**–**c**) Photographs of the spongy structure of the fracture surface at different magnifications; (**d**) Photograph of the fractured head part at low magnification with a large number of cracks observed on the surface.

4. Discussion

In this section, we discuss the results of the dynamic flow stress assessment for classical and profiled cylinders. Each individual experiment with the 4 mm profiled cylinder can be used to calculate the dynamic flow stress and strain rate using Equations (1), (4), and (5). On the other hand, each individual result can depend on the local fluctuations in microstructure and mechanical properties of the material, as well as the imperfections of particular tests. Therefore, statistically based estimation is more valid for averaged representation of material properties [16,18]. To do this, here, we adopt a statistical Bayesian approach to calculate the dynamic flow stress.

The strain rate varies by 2–3 times in the considered interval of impact velocities, and the dynamic flow stress can be assumed to be a constant in such relatively narrow range of strain rates. For a given flow stress Y, one can estimate the final length of the head part using Equation (2) at $v = 0$ and knowing all other parameters of the sample. Performing such calculations for all experimental points, we obtained the model-estimated lengths and the sum of squares of their deviations from the experimentally measured ones, which is an inverse measure of the likelihood of this value of Y. Randomly seeding Y multiple times in the range from 0 to 1500 MPa, we choose the optimal flow stress as that provides the minimum value of the sum of squares of deviations. In the case of 7075 alloy, this procedure gives an optimal value of $Y = 786$ MPa, which ensures a close fit of the final lengths of the head part for most of the samples as shown in Figure 9a. This value also corresponds to particular estimates of the dynamic flow stress based on individual experiments as shown in Figure 9c. Interestingly, there are two out-of-dependence individual points with higher flow stresses of about 1100 MPa in Figure 9c. A probable reason is a local increase in strength due to fluctuations of material microstructure. Another probable explanation is a technical issue of the overestimation of strength because of bending of the head part in these experiments, see Figure 4a. On the other hand, previous MD simulations [29] showed that bending of the head part can take place even in the context of perfect sample shape and ideally normal impact due to material anisotropy or heterogeneity. Therefore, in the experiments, this bending can also be provoked by a local heterogeneity, namely, the areas of higher strength.

In the case of V95T1 alloy, we have fewer experiments with non-fractured 4 mm profiled samples showing substantial scatter. Specifically, the sample impacted at 87 m/s reveals much lower flow stress (Figure 9d) and much severe deformation (Figure 4b) than expected. Therefore, the optimization was performed for all four experimental points giving a low value of $Y = 450$ MPa and only for the first three experiments giving a more reasonable value of $Y = 624$ MPa as shown in Figure 9d,f. On the one hand, the deviating point can result from local microstructure fluctuation. On the other hand, it can reveal strain softening as a precursor of fracture.

In Figure 9e,f, the impact velocity is recalculated into the strain rate using Equations (4) and (5) for the profiled samples. One can conclude that the experiments with the profiled 4 mm samples correspond to a range of strain rates of (4–8) $\times\, 10^3$ s^{-1} for 7075 alloy and the close range of (2–6) $\times\, 10^3$ s^{-1} for V95T1 alloy. Although individual estimates show some tendency for strain rate softening at high velocities close to the fracture threshold, we do not have enough statistically based information to be sure about this softening and can suppose a constant dynamic flow stress in this range of strain rates as the simplest hypothesis.

Figure 10 compares the statistically based estimates of the flow stress obtained for 4 mm profiled samples with the individual estimates for 8 mm classical samples calculated using Equation (6). This comparison shows that the previously obtained estimates of $Y = 786$ MPa for 7075 alloy and $Y = 624$ MPa for V95T1 alloy correlates well with the main part of the individual 8 mm data points. At the same time, the lower estimate of 450 MPa for V95T1 alloy definitely underestimates the flow stress; therefore, we disregard this value. Interestingly, some of individual estimates show higher flow stress exceeding 1000 MPa, which correlates with the results for profiled samples. However, the classical ones are not prone to bending, see Figure 3. This finding supports our previous conclusion about the local microstructural heterogeneities of both alloys.

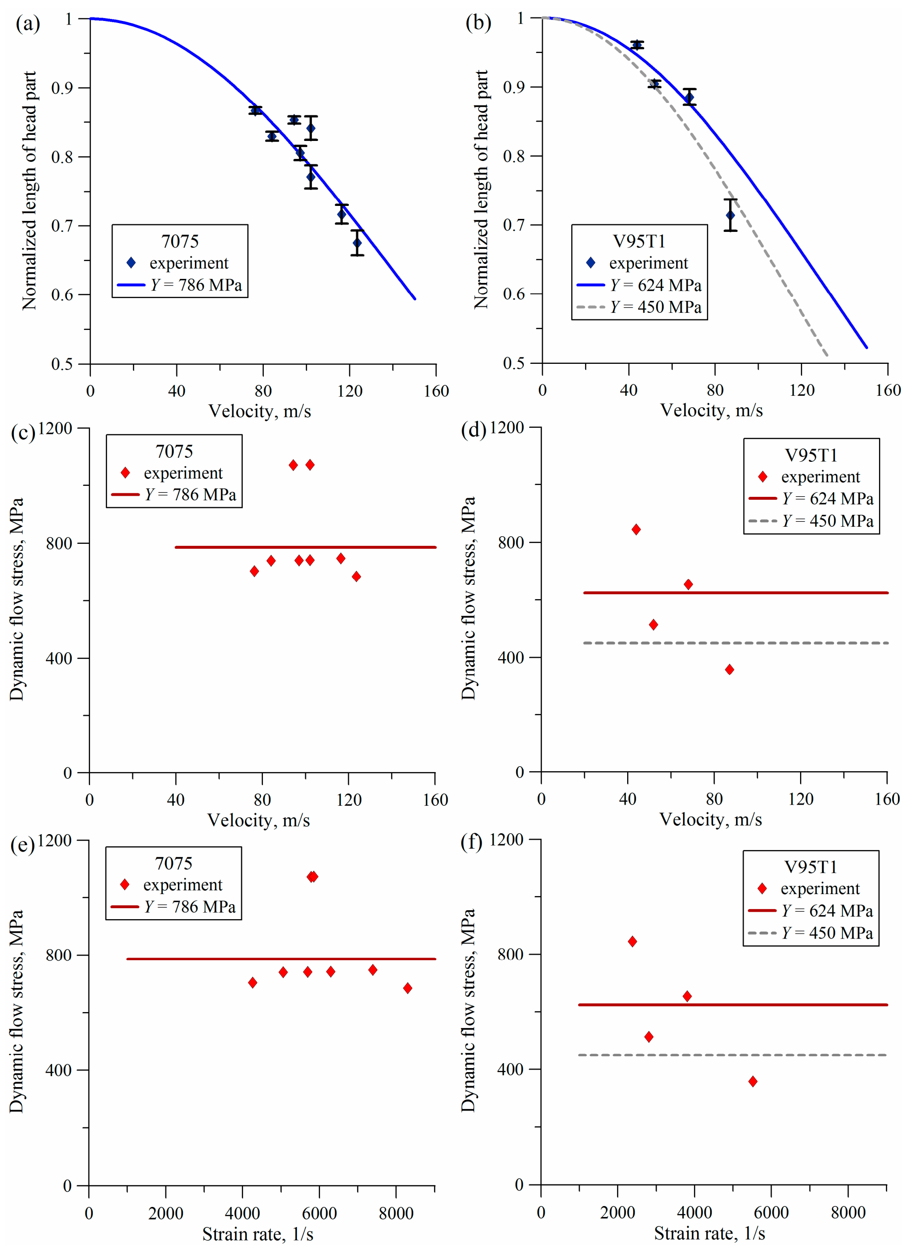

Figure 9. Dynamic flow stress of aluminum alloys calculated using the experimental results for 4 mm profiled cylinders: (**a**) Fitting of the yield stress to the dependencies of the final normalized length of the head part on the impact velocity for 7075 alloy; (**b**) The same for V95T1 alloy; (**c**) Estimates of the flow stress from individual experiments as compared with the optimized level plotted versus impact velocity for 7075 alloy; (**d**) The same for V95T1 alloy; (**e**) The same plot versus strain rate velocity for 7075 alloy; (**f**) The same for V95T1 alloy.

The fitted curves in Figure 9 for the final length of the head part of the 4 mm profiled samples were recalculated in the engineering strain $\varepsilon_f = 1 - L_{hf}/L_{h0}$ and used for determination of the fracture strain as shown in Figure 11. In the case of 7075 alloy, the samples impacted at 116.3 m/s and 131.5 m/s were fractured, while another sample impacted at 116.3 m/s and that impacted it 123.5 m/s remained intact, see Figure 4. Therefore, the dynamic fracture strain of 7075 aluminum alloy at 8×10^3 s^{-1} can be estimated to be in the range 0.27–0.33, while the specific value depends on the local microstructure. In the case of V95T1 alloy, all samples with impact velocities above 108 m/s were fractured, but an uncertainty arises from possible softening before fracture. As a result, the dynamic fracture strain of V95T1 aluminum alloy at 6×10^3 s^{-1} can be estimated to be in the range of 0.29–0.36. Interestingly, although the threshold velocity of fracture is definitely lower for V95T1 alloy, the fracture strain is close or even slightly higher than that for 7075 alloy. This feature results from lower dynamic flow stress and, correspondingly, more severe deformation of V95T1 samples at the same impact velocity. Thus, we can conclude that V95T1 aluminum alloy is less strong but more ductile, while 7075 aluminum alloy is stronger but, simultaneously, more brittle. This conclusion is in line with the fracture pattern shown in Figures 4 and 5. The stress concentrators near the transition between the reduced head part and the main part provokes breaking off of the head part in the brittle 7075 alloy. In the ductile V95T1 alloy, the fracture goes along the shear direction, and the stress concentrators are not so dangerous. All estimated parameters of both alloys are collected in Table 2.

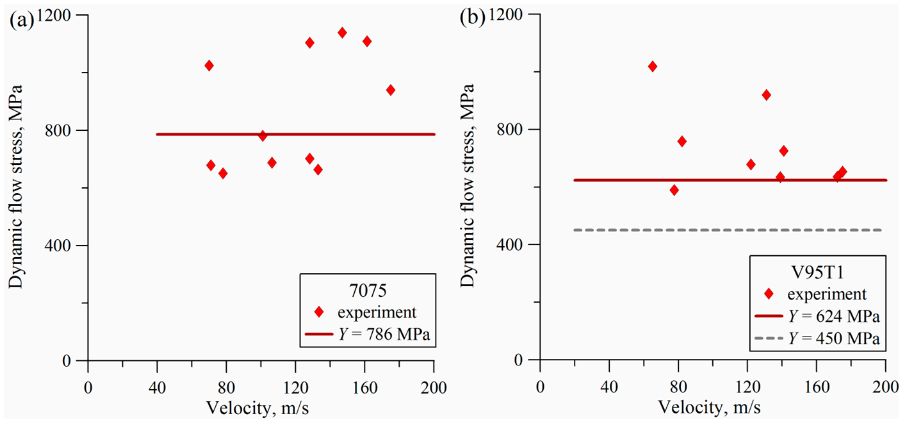

Figure 10. Dynamic flow stress of aluminum alloys calculated using the experimental results for 8 mm classical uniform cylinders made of the following: (**a**) 7075 alloy; (**b**) V95T1 alloy. Estimates of the flow stress from individual experiments are plotted versus impact velocity in comparison with the optimization results for 4 mm profiled cylinders (horizontal lines).

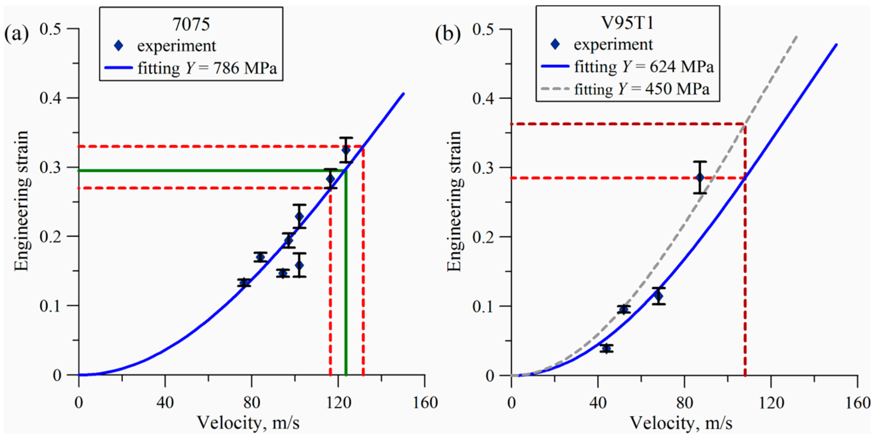

Figure 11. Estimation of fracture strain for the following: (**a**) 7075 alloy; (**b**) V95T1 alloy. Experimental engineering strains are plotted versus the impact velocity together with their fittings in approximation of constant flow stress. Velocities of the experimentally fractured samples (vertical lines) and the corresponding strain levels (horizontal lines) are noted by red dashed lines, while an intermediate intact 7075 sample is noted by solid greed lines.

Table 2. Measured dynamic mechanical properties of 7075 and V95T1 alloys.

Parameter	Al 7075	V95T1
Strain rate range, s^{-1}	$(4–8) \times 10^3$	$(2–6) \times 10^3$
Dynamic flow stress, MPa	786	624
Dynamic fracture strain	0.27–0.33	0.29–0.36

Let us compare our results with the literature data. Feng et al. [34] reported an ultimate compressive strength of about 670 MPa, an average flow stress of about 570 MPa, and a fracture strain of about 0.45 for AA7075-T4 aluminum alloy compressed at room temperature with a low strain rate of 0.1 s^{-1}. A tensile strength of about 600 MPa and a much lower fracture strain of about 0.1 was reported by Leng et al. [35] for solution heat-treated and aged 7075 aluminum alloy at quasi-static tension with a strain rate of 0.001 s^{-1}. For 7075 aluminum alloy subjected to T651 solution heat treatment, Wang et al. [36] reported a quasi-static flow stress at 0.001 s^{-1} of about 530 MPa. The same authors performed impact experiments with 2 mm samples and a flyer plate at impact velocities ranging from 155 to 340 m/s, which corresponds to the strain rate by an order of 10^5 s^{-1}. They found a Hugoniot elastic limit of about 650 MPa, which can be recalculated into a dynamic yield strength of about 540 MPa. Due to restricted strain values at plane shock loading, this value corresponds to an initial stage of compressive deformation without substantial work hardening. Peng et al. [37] reported a tensile fracture strain of about 0.13 and an ultimate tensile strength in the range of 580−650 MPa depending on aging time for commercial 7075 alloy after solution heat treatment and following aging; split Hopkinson pressure bar was used with a tensile strain rate of about 2.4×10^3 s^{-1}. All these data are quite consistent with our results for the dynamic compression of 7075 aluminum alloy reported in Table 2 considering the difference in strain rate, deformation level, and deformation mode (tension/compression). In addition, the literature data on substantial variation in mechanical properties depending on preliminary thermo-mechanical treatment explains the measured differences in properties between 7075 and V95T1 alloys based on possible variations in the thermo-mechanical treatment rather than in the chemical composition.

5. Conclusions

A novel method to measure dynamic flow stress and corresponding strain rate in Taylor tests using profiled samples with a reduced cylindrical head part was applied to study dynamic characteristics of similar commercial 7075 and V95T1 aluminum alloys. The measured dynamic flow stress is verified using a classical Taylor's approach with uniform cylinders and compared with the literature data. Our study shows that the dynamic flow stress of 7075 alloy, which is 786 MPa at strain rates of (4–8) $\times 10^3$ s^{-1}, exceeds that of 624 MPa for V95T1 alloy at the strain rates of (2–6) $\times 10^3$ s^{-1} by 25%. The threshold impact velocity resulting in fracture of the 4 mm head part of the profiled samples is 116–130 m/s for 7075 alloy and only 108 m/s for V95T1 alloy. The fracture pattern is also different between the alloys with characteristic shear-induced cracks oriented at 45° to the impact direction in the case of V95T1 alloy and perpendicular to the breaking off head part in the case of 7075 alloy. On the other hand, the compressive fracture strain of V95T1 alloy, which is 0.29–0.36, exceeds that of 7075 alloy, which is 0.27–0.33, by approximately 8%. Thus, we can conclude that V95T1 aluminum alloy is less strong but more ductile, while 7075 aluminum alloy is stronger but, simultaneously, more brittle. Given the close chemical composition of both alloys, see Table 1, we assume that the difference in dynamic properties is related to different thermo-mechanical treatments during production.

Author Contributions: Conceptualization, E.S.R., P.N.M. and A.E.M.; methodology, E.S.R., V.G.L. and A.E.M.; software, E.S.R. and A.E.M.; validation, E.S.R., A.Y.C., T.T.S. and A.E.M.; formal analysis, E.S.R., A.Y.C., T.T.S. and A.E.M.; investigation, E.S.R., A.Y.C., A.G.F. and T.T.S.; resources, E.S.R., A.G.F., V.G.L. and P.N.M.; data curation, E.S.R. and A.Y.C.; writing—original draft preparation, E.S.R.; writing—review and editing, A.E.M.; visualization, E.S.R. and A.G.F.; supervision, A.E.M.; project administration, P.N.M.; funding acquisition, P.N.M. All authors have read and agreed to the published version of the manuscript.

Funding: This research was funded by the Russian Science Foundation, grant number 24-19-00684, https://rscf.ru/en/project/24-19-00684/ (accessed on 10 February 2025).

Data Availability Statement: The original contributions presented in this study are included in the article. Further inquiries can be directed to the corresponding author(s).

Conflicts of Interest: The authors declare no conflicts of interest. The funders had no role in the design of the study; in the collection, analyses, or interpretation of data; in the writing of the manuscript; or in the decision to publish the results.

Abbreviations

The following abbreviations are used in this manuscript:

MD	Molecular dynamics
SEM	Scanning electron microscopy

Appendix A

Table A1 collects the experimentally measured lengths of the dynamically deformed samples and diameters of the impact edge for all tested samples except those revealing fractures. The average values and error ranges are determined using six measurements for each parameter.

Table A1. Measured geometric parameters of the impacted samples without fracture.

Impact Velocity (m/s)	Length (mm)	Diameter (mm)
	Al 7075	
	Classical 8 mm specimens	
70	39.68 ± 0.07	8.18 ± 0.05
71	39.43 ± 0.09	8.22 ± 0.02
78	39.49 ± 0.05	8.28 ± 0.02
101	39.38 ± 0.08	8.48 ± 0.02
106.4	37.29 ± 0.06	8.54 ± 0.04
128.2	38.92 ± 0.07	8.95 ± 0.04
128.2	39.09 ± 0.15	8.93 ± 0.04
133	38.83 ± 0.06	9.03 ± 0.05
147	39.15 ± 0.1	9.23 ± 0.02
161.3	38.9 ± 0.22	9.56 ± 0.04
175	38.01 ± 0.13	9.54 ± 0.02
	Profiled 4 mm specimens	
76.3	38.18 ± 0.02	4.28 ± 0.03
84	38.25 ± 0.04	4.3 ± 0.02
94.3	37.83 ± 0.02	4.56 ± 0.04
97	38.07 ± 0.08	4.7 ± 0.04
102	37.26 ± 0.12	4.68 ± 0.03
102	38.32 ± 0.14	4.61 ± 0.06
116.3	37.06 ± 0.09	5.18 ± 0.03
123.5	36.29 ± 0.12	5.13 ± 0.04
	Al V95T1	
	Classical 8 mm specimen	
65	39.91 ± 0.09	8.16 ± 0.06
77.5	39.19 ± 0.04	8.17 ± 0.04
82	39.57 ± 0.02	8.16 ± 0.02
122	39.18 ± 0.04	8.64 ± 0.05
131	37.89 ± 0.05	8.86 ± 0.05
139	38.13 ± 0.11	9.03 ± 0.04
141	38.8 ± 0.03	8.96 ± 0.02
172	38.08 ± 0.05	9.77 ± 0.06
175	36.35 ± 0.03	9.94 ± 0.07
	Profiled 4 mm specimen	
43.8	39.53 ± 0.02	4.17 ± 0.02
51.8	38.97 ± 0.02	3.93 ± 0.08
68	38.88 ± 0.09	4.39 ± 0.04
87	37.17 ± 0.16	4.51 ± 0.02

References

1. Bilalov, D.A.; Sokovikov, M.A.; Chudinov, V.V.; Oborin, V.A.; Bayandin, Y.V.; Terekhina, A.I.; Naimark, O.B. Numerical simulation and experimental study of plastic strain localization under the dynamic loading of specimens in con-ditions close to a pure shear. *J. Appl. Mech. Tech. Phys.* **2018**, *59*, 1179–1188. [CrossRef]
2. Nguyen, T.; Fensin, S.J.; Luscher, D.J. Dynamic crystal plasticity modeling of single crystal tantalum and validation using Taylor cylinder impact tests. *Int. J. Plast.* **2021**, *139*, 102940. [CrossRef]
3. Jeong, Y.-M.; Hong, S.; Won, J.Y.; Kim, C.; Lee, M.-G. A Practical inverse identification of Johnson–Cook parameters at intermediate strain rates using split Hopkinson pressure bar test. *Met. Mater. Int.* **2024**, *30*, 2093–2109. [CrossRef]
4. Kanel, G.I.; Razorenov, S.V.; Baumung, K.; Singer, J. Dynamic yield and tensile strength of aluminum single crystals at temperatures up to the melting point. *J. Appl. Phys.* **2001**, *90*, 136–143. [CrossRef]
5. Winey, J.M.; LaLone, B.M.; Trivedi, P.B.; Gupta, Y.M. Elastic wave amplitudes in shock-compressed thin polycrystalline aluminum samples. *J. Appl. Phys.* **2009**, *106*, 073508. [CrossRef]
6. Gurrutxaga-Lerma, B.; Shehadeh, M.A.; Balint, D.S.; Dini, D.; Chen, L.; Eakins, D.E. The effect of temperature on the elastic precursor decay in shock loaded FCC aluminium and BCC iron. *Int. J. Plast.* **2017**, *96*, 135–155. [CrossRef]
7. Saveleva, N.V.; Bayandin, Y.V.; Savinykh, A.S.; Garkushin, G.V.; Razorenov, S.V.; Naimark, O.B. The formation of elastoplastic fronts and spall fracture in AMg6 alloy under shock-wave loading. *Tech. Phys. Lett.* **2018**, *44*, 823–826. [CrossRef]
8. Barker, L.M.; Hollenbach, R.E. Laser interferometer for measuring high velocities of any reflecting surface. *J. Appl. Phys.* **1972**, *43*, 4669–4675. [CrossRef]
9. Moćko, W.; Janiszewski, J.; Radziejewska, J.; Grązka, M. Analysis of deformation history and damage initiation for 6082-T6 aluminium alloy loaded at classic and symmetric Taylor impact test conditions. *Int. J. Impact. Eng.* **2015**, *75*, 203–213. [CrossRef]
10. Pakhnutova, N.V.; Boyangin, E.N.; Shkoda, O.A.; Zelepugin, S.A. Microhardness and dynamic yield strength of copper samples upon impact on a rigid wall. *Adv. Eng. Res.* **2022**, *22*, 224–231. [CrossRef]
11. Zelepugin, S.A.; Pakhnutova, N.V.; Shkoda, O.A.; Boyangin, E.N. Experimental study of the microhardness and microstructure of a copper specimen using the Taylor impact test. *Metals* **2022**, *12*, 2186. [CrossRef]
12. Rodionov, E.S.; Lupanov, V.G.; Grachyova, N.A.; Mayer, P.N.; Mayer, A.E. Taylor impact tests with copper cylinders: Experiments, microstructural analysis and 3D SPH modeling with dislocation plasticity and MD-informed artificial neural network as equation of state. *Metals* **2022**, *12*, 264. [CrossRef]
13. Xu, J.; Liu, Q.; Xu, Y.F.; Guo, S.H.; Li, C.; Zhang, N.B.; Cai, Y.; Liu, X.Y.; Lu, L.; Luo, S.N. Taylor impact of high-entropy alloy $Al_{0.1}CoCrFeNi$: Dynamic severe plastic deformation and bulk gradient structure. *J. Alloys Compd.* **2023**, *936*, 168261. [CrossRef]
14. Taylor, G.I. The use of flat-ended projectiles for determining dynamic yield stress. I. Theoretical considerations. *Proc. R. Soc. Lond. Ser. A Math. Phys. Eng. Sci.* **1948**, *194*, 289–299. [CrossRef]
15. Rivera, D.; Bernstein, J.; Schmidt, K.; Muyskens, A.; Nelms, M.; Barton, N.; Kupresanin, A.; Florando, J. Bayesian calibration of strength model parameters from Taylor impact data. *Comput. Mater. Sci.* **2022**, *210*, 110999. [CrossRef]
16. Rodionov, E.S.; Pogorelko, V.V.; Lupanov, V.G.; Mayer, P.N.; Mayer, A.E. Modified Taylor impact tests with profiled copper cylinders: Experiment and optimization of dislocation plasticity model. *Materials* **2023**, *16*, 5602. [CrossRef] [PubMed]
17. Zelepugin, S.A.; Cherepanov, R.O.; Pakhnutova, N.V. Optimization of Johnson–Cook constitutive model parameters using the nesterov gradient-descent method. *Materials* **2023**, *16*, 5452. [CrossRef]
18. Rodionov, E.S.; Pogorelko, V.V.; Lupanov, V.G.; Fazlitdinova, A.G.; Mayer, P.N.; Mayer, A.E. Dynamic deformation and fracture of brass: Experiments and dislocation-based model. *Int. J. Plast.* **2024**, *183*, 104165. [CrossRef]
19. Rodionov, E.S.; Mayer, A.E. Estimation of dynamic yield stress by Taylor test with reduced cylindrical head part of samples. *Chelyabinsk Phys. Math. J.* **2023**, *8*, 399–409. [CrossRef]
20. Khalid, M.Y.; Umer, R.; Khan, K.A. Review of recent trends and developments in aluminium 7075 alloy and its metal matrix composites (MMCs) for aircraft applications. *Results Eng.* **2023**, *20*, 101372. [CrossRef]
21. Liu, L.; Zhao, G.; Wang, G.; Ma, X.; Yan, Z.; Cao, S. Hot deformation behavior and microstructure evolution model of 7055 aluminum alloy. *J. Mater. Res. Technol.* **2023**, *27*, 3191–3213. [CrossRef]
22. Wu, J.-F.; He, D.-G.; Lin, Y.C.; Chen, Z.-J.; Ding, H.-B.; Qiu, Y.-L. A unified constitutive model and microstructure evolution of a solution treated 7075 aluminum alloys under warm forming condition. *J. Mater. Res. Technol.* **2024**, *30*, 4159–4168. [CrossRef]
23. Ye, T.; Xia, E.; Qiu, S.; Liu, J.; Yue, H.; Tang, J.; Wu, Y. Deformation behavior of an extruded 7075 aluminum alloy at elevated temperatures. *Materials* **2024**, *17*, 1210. [CrossRef] [PubMed]
24. Hua, L.; Zhou, P.; Song, Y.; Sun, Q. Characterization of strain rate sensitivity of 7075 aluminum alloy at different solution temperatures by novel kinetic models. *Mater. Sci. Eng. B* **2022**, *282*, 115751. [CrossRef]
25. Fu, R.; Liang, Y.; Han, Q.; Guo, Y.; Lei, H.; Liu, C. Strengthening and fracturing mechanisms of laser-directed energy deposited Al-7075 alloy. *Mater. Sci. Eng. A* **2023**, *881*, 145433. [CrossRef]
26. Praveen, R.; Koteswara Rao, S.R.; Kumar, S.S.; Rajesh Babu, T. Numerical evaluation of ballistic limit velocity and experimental ballistic response of 25 mm thick aluminium 7075 alloy targets. *Mater. Today Proc.* **2022**, *62*, 523–529. [CrossRef]

27. Praveen, R.; Koteswara Rao, S.R.; Selvakumar, G.; Damodaram, R. High-velocity projectile impact behaviour of friction stir welded AA7075 thick plates. *Def. Technol.* **2023**, *29*, 153–163. [CrossRef]
28. Ohno, M.; Yamashita, M.; Matsuura, K. Importance of microstructural evolution on prediction accuracy of microsegregation in Al-Cu and Fe-Mn alloys. *Int. J. Heat Mass Transf.* **2019**, *132*, 1004–1017. [CrossRef]
29. Mayer, A.E.; Rodionov, E.S.; Pogorelko, V.V.; Mayer, P.N. Molecular dynamics simulations of Taylor impact tests with classical and profiled copper cylinders. *Chelyabinsk Phys. Math. J.* **2025**, *10*.
30. Gholami, M.D.; Salamat, M.; Hashemi, R. Study of mechanical properties and wear resistance of Al 1050/Brass (70/30)/Al 1050 composite sheets fabricated by the accumulative roll bonding process. *J. Manuf. Process.* **2021**, *71*, 407–416. [CrossRef]
31. Qu, S.; Yao, G.; Tian, J.F.; Zhang, Z.F. Failure analysis of the brass tubes in a lubricating oil cooler. *Eng. Failure Anal.* **2011**, *18*, 2232–2239. [CrossRef]
32. Liu, L.; Chi, R. Effect of microstructure on high cycle fatigue behavior of brass processed by laser shock peening. *Mater. Sci. Eng. A* **2019**, *740–741*, 342–352. [CrossRef]
33. Shahmirzaloo, A.; Hosseini, S.M.; Siahsarani, A.; Rahmatabadi, D.; Hashemi, R.; Faraji, G. Influences of the constrained groove pressing on microstructural, mechanical, and fracture properties of brass sheets. *Mater. Res. Express* **2020**, *7*, 116526. [CrossRef]
34. Feng, Z.; Liu, C.; Ma, P.; Yang, J.; Chen, K.; Li, G.; Chen, L.; Huang, Z.J. Initial holding time dependent warm deformation and post-ageing precipitation in an AA7075-T4 aluminum alloy. *Mater. Process. Technol.* **2021**, *294*, 117111. [CrossRef]
35. Leng, L.; Zhang, Z.J.; Duan, Q.Q.; Zhang, P.; Zhang, Z.F. Improving the fatigue strength of 7075 alloy through aging. *Mater. Sci. Eng. A* **2018**, *738*, 24–30. [CrossRef]
36. Wang, X.; Wang, G.; Nan, X.; Ma, C.; Jiang, Z.; Hu, J.; Wang, Y. Mechanical behavior and microstructure evolution of different aluminum materials under shock loading. *J. Mater. Res. Technol.* **2024**, *29*, 3614–3625. [CrossRef]
37. Peng, W.; Gao, Y.; Li, H.; Lu, L.; Ma, K.; Lin, L.; Shao, Y.; Shi, T. Effects of different initial states on dynamic tensile properties and microstructure of 7075 aluminum alloy. *Mater. Sci. Eng. A* **2024**, *891*, 145939. [CrossRef]